Viscosity-Dependent Internal Variability in a Model of the North Pacific

JORDAN T. DAWE AND LUANNE THOMPSON

Department of Oceanography, University of Washington, Seattle, Washington

(Manuscript received 4 February 2004, in final form 16 September 2004)

ABSTRACT

A 2°-resolution isopycnal model of the North Pacific Ocean is shown to produce anomalies that propagate around the subtropical gyre on the decadal time scale that do not appear in a 1°-resolution version of the same model. A principal oscillation pattern (POP) analysis of the isopycnal interface anomaly is performed to examine the dynamics responsible for the anomaly generation. The POPs show a coherent oscillation around the entire subtropical gyre with two centers of action, one in the Central Mode Water (CMW) region, the other in the Subtropical Countercurrent (STCC). Lead–lag covariances between the subduction rate in the CMW and the layer thickness along the oscillation path indicate that anomalous subduction events are not the driving mechanism for the oscillation. A linearized quasigeostrophic mode analysis shows that the anomalies are generated by flow instability in the region of the STCC. The instability disappears in the 1° model because of changes in the horizontal viscosity, which is set in each model to the minimum value necessary to resolve the western boundary current and preserve numerical stability. A criterion for model resolution of an instability of a given length and time scale damped by biharmonic viscosity is derived. The enhancement of the large-scale instabilities in the low-resolution model emphasizes the importance of achieving mesoscale resolution in ocean models used for climate studies.

1. Introduction

There is continuing debate over whether the midlatitude ocean plays an important role in the decadal variability of the climate system. The debate centers on whether there exists a climate signal that rises above the red noise spectrum expected from the interaction of the noisy atmosphere with the more sluggish ocean (Frankignoul 1985; Dommenget and Latif 2002). Such a signal could potentially appear because of the ability of the ocean to store heat on a variety of time scales. Stored heat could eventually be released back to the atmosphere years later, causing long-term feedbacks that would influence the climate on decadal time scales.

One possible way the long time scale could come about is through a coupled mode of ocean–atmosphere interaction. This has been suggested mechanistically by Gu and Philander (1997), who discuss the subduction of midlatitude temperature anomalies that eventually influence tropical SST, and through a coupled ocean–atmosphere model by Latif and Barnett (1994), where the delayed mechanism occurs through the adjustment of the gyre by long Rossby waves and advection in the western boundary current. Most studies of climate variability focus on these types of atmosphere–ocean interaction, but it is also possible that oscillations intrinsic to the ocean could create decadal variability that forces changes in the atmosphere without atmospheric feedback on the ocean.

It is well known that baroclinic instability provides a source of internal oceanic variability on weekly to monthly time scales. In the North Pacific Ocean, for instance, the Kuroshio displays high levels of eddy variability due to the baroclinic instability of the current (Tai and White 1990; Qiu 2002). The Subtropical Countercurrent (STCC) also displays high levels of seasonably modulated variability, apparently due to a kind of baroclinic instability acting in the upper thermocline (Qiu 1999; Kobashi and Kawamura 2001). Longer-term modes of oceanic variability are difficult to detect in the limited amount of data collected in the last century, and so we must turn to numerical models to study time scales longer than the seasonal.

Ocean-only models have been shown to internally generate variability that has interannual to decadal time scales. Cox (1987) identified interannual mode water variations in an idealized subtropical gyre model. The forcing for these oscillations was attributed to variations in the location and amount of subduction in the western boundary current extension. Hazeleger and Drijfhout (2000) studied an oscillation in an idealized, high-horizontal resolution isopycnal model of the North Atlantic Ocean. They found two modes of variability in the Subtropical Mode Water, with characteristic periods of 4.5 and 8 yr. Based on a model study,

Corresponding author address: Jordan T. Dawe, University of Washington, School of Oceanography, Box 355351, Seattle, WA 98195.
E-mail: freedryk@ocean.washington.edu

Qiu and Miao (2000) suggest that decadal-scale changes in the mean path of the Kuroshio off Japan are due to internal dynamics. The transitions between meander and nonmeander states in the Kuroshio have significant impacts on the fluid transport, and thus the heat transport, of the Kuroshio, and on the extent and energetics of the Kuroshio Extension (Qiu 2000). Decadal-scale oscillatory variability in an idealized ocean model was also observed by Colin de Verdiere and Huck (1999), forced by the interaction between heat flux restoration to atmospheric conditions and baroclinic instability.

Because of the relative coarseness of the grid spacing and the parameterizations of small-scale processes used in constructing ocean models, it is difficult to assess the accuracy of these simulations. Indeed, several authors have shown that the choice of vertical discretization scheme (Griffiths et al. 2000), vertical resolution (Wood and Ikeda 1994), horizontal resolution (Böning and Budich 1992; Drijfhout 1992), viscosity (Best et al. 1999), or continuity equation (Griffiths et al. 2000) can all alter the dynamics of baroclinic instability and the resulting eddy field. These errors and inaccuracies in ocean models are a continuing source of difficulty in the interpretation of climate model results.

This study examines an oscillation that takes place in an isopycnal model of the North Pacific, driven by instability in the westward flow of the subtropical gyre. The oscillation is shown to be dependent on the model's horizontal viscosity, with the oscillation amplitude decreasing as viscosity is decreased. Since the need to resolve the western boundary current and preserve numerical stability defines a resolution-dependent minimum model viscosity, this implies that inadequate resolution may not only suppress small-scale variability; it may actually enhance variability on the large scale.

Following a brief description of the model used in this study, we present the model oscillation in section 3 and perform a principal oscillation pattern (POP) analysis to examine the oscillation's characteristics. Also in section 3, we look at the subduction anomalies associated with the oscillation in the Central Mode Water region. In section 4, we analyze the linearized quasigeostrophic instability characteristics of the southern part of the model's subtropical gyre and the effects of horizontal grid spacing and viscosity on the unstable modes. In section 5 we derive a condition for model resolution of a quasigeostrophic instability damped by a biharmonic viscosity. We summarize the results and implications of this study in section 6.

2. Model description

The Hallberg Isopycnal Model (HIM; Hallberg 1995; Ladd and Thompson 2002) was used in this study. This primitive equation model consists of an isopycnal interior coupled to an Oberhuber-type mixed layer (Oberhuber 1993). A biharmonic viscosity scheme is used, with a constant viscosity set to the minimum necessary to resolve the western boundary current. A fully nonlinear equation of state is implemented in the model, as well as bulk formulas for latent and sensible heat flux forcing (Zeng et al. 1998). Short- and longwave radiation is interpolated from Da Silva monthly climatological values (Da Silva et al. 1994), as are the atmospheric variables used in the bulk formulas. Sea surface salinity (SSS) is restored to the *WOA94* (Levitus et al. 1994) monthly climatology with a 1-month *e*-folding time.

The model domain stretches from 20°S to 70°N and from 100°E to 90°W. Sponge layers at the southern and northern boundaries relax layer temperature, salinity, and interface depth to climatology in order to simulate open boundaries. The model has realistic bottom topography and coastlines taken from the ETOPO dataset. The topography data are mapped to the model grid, filtered with a three-point smoother, a maximum ocean depth of 6000 m is enforced, and points shallower than 20 m are assumed to be land.

The model consists of two deep isopycnal layers that have no direct atmospheric contact, six isopycnal layers representing the outcropping thermocline, and the two-layer mixed layer model that has continuously variable density in the horizontal. The isopycnal σ_θ values were chosen to resolve the densities of the Subtropical, Central, and Eastern Mode Waters: 24, 25, 25.6, 26, 26.5, 26.9, 27.5, and 27.7 σ_θ. The initial density structure is taken from the *WOA94* (Levitus et al. 1994; Levitus and Boyer 1994).

Two main runs were performed at 1° and 2° grid resolution and the patterns of interannual variability compared. The only model parameters that were changed between these runs were the time step, which was shortened at 1° resolution to satisfy the CFL criterion, and the horizontal viscosity, which was larger at 2° resolution in order to resolve the western boundary current. The viscosity was set to 1.5×10^{15} m^4 s^{-1} for the 2° model and 4.1×10^{13} m^4 s^{-1} for the 1° model.

The model was spun up for 50 yr, then run for 50 yr and the output analyzed. The model does a good job of reproducing the isopycnal structure and circulation of the North Pacific with the exception of the Kuroshio Extension, which separates from Japan ~5° too far north, as is common in low-resolution models. This has the effect of deepening the subtropical thermocline; the density of the Subtropical Mode Water is shifted to the 26-σ_θ isopycnal, and the thickness of the 26.5-σ_θ isopycnal is increased, more than doubling in the central Pacific. This error is reduced at 1° resolution relative to 2° resolution.

3. Model oscillation

a. Oscillation description

The 2° model output displays a series of layer thickness anomalies propagating around the subtropical gyre (Figs. 1a, c). These anomalies are striking in both their

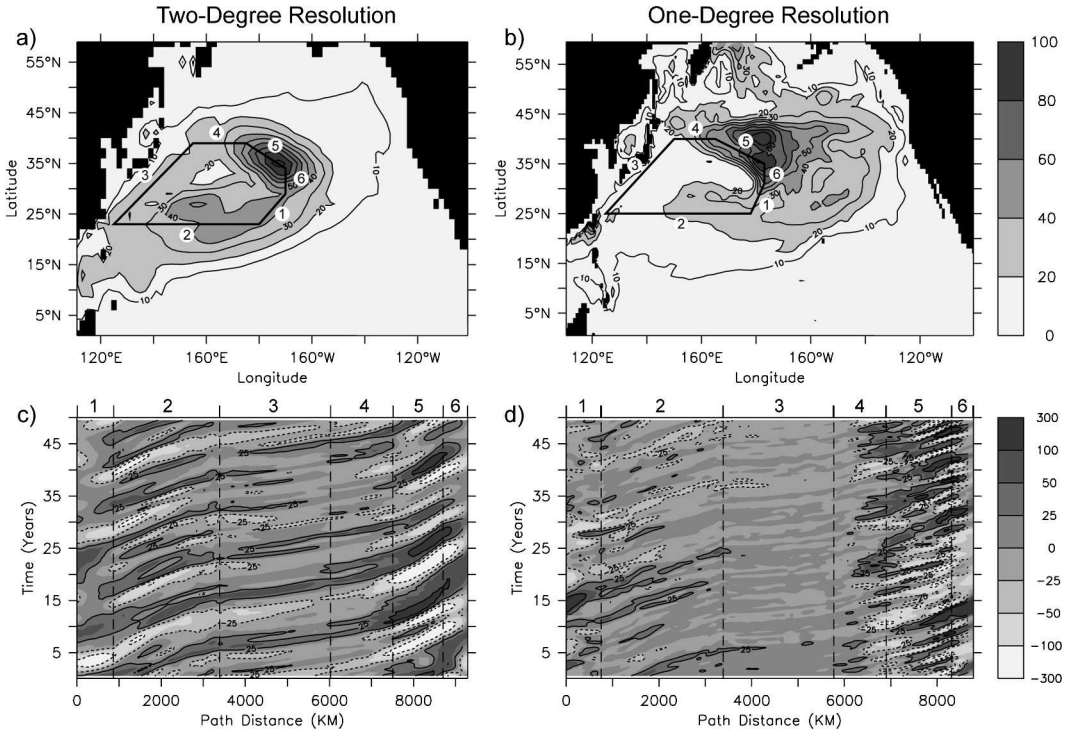

FIG. 1. (a) Standard deviation of 26.5-σ_θ layer thickness (m) for 2° model. A representative path for the oscillation is drawn in black. Path sections are numbered to correspond with numbered sections in (c). (b) Same as (a), but for the 1° model. Path sections are numbered to correspond with numbered sections in (d). (c) Time–path plot of 26.5-σ_θ thickness anomaly (m) in the 2° model along the path defined on the standard deviation map, starting at 30°N, 170°W and proceeding clockwise. Vertical black dashed lines mark turns in the path, and each section is numbered as in (a). The data have been smoothed in time with a 13-point Hanning filter. (d) Same as (c), but for the 1° model. Each path section is numbered as in (b).

size and persistence. They appear largest on the 26.5-σ_θ isopycnal, starting near 25°N, 160°W. The anomalies move westward between 20° and 30°N until they reach the western boundary. There the anomalies split, either propagating along the coast toward the equator while rapidly dissipating, or becoming entrained into the Kuroshio and advecting northward into the Kuroshio Extension. There they enter the wintertime outcrop area of the Central Mode Water and emerge heading southwest. Layer thickness at a given point along the anomaly path oscillates on an ~10 yr time scale, and it takes ~25 yr for an individual anomaly to complete a circuit around the gyre.

Although still displaying an anomaly pattern that travels around the gyre, the 1° model has a much-reduced magnitude when compared with the 2° model (Figs. 1b,d). Thickness anomalies created in the eastern gyre tend to dissipate rapidly as they head westward, and they rarely make it past 160°E. The Kuroshio is much tighter against the western boundary and displays a recirculation flow that makes it difficult for anomalies with a sizeable horizontal extent to be entrained into the Extension region. The large anomalies in the Central Mode Water region are also much less organized than in the 2° run and have broken into two regions.

Two other runs were performed at 2° resolution to examine the effect of different model configurations on the oscillation. First, the vertical resolution of the model was increased to 30 layers. This resulted in the anomalies roughly halving in horizontal spatial size, but the other details of the oscillation were basically unchanged. Second, the mean annual heat fluxes were calculated using the bulk algorithms, and these mean fluxes were used to force a run, thus removing possible feedbacks between SST and heat flux. This had little effect on the oscillation, establishing that it is generated by physics intrinsic to the ocean.

b. *Principal oscillation pattern analysis*

To quantify the vertical structure and oscillatory time scale of the anomalies, a principal oscillation pattern analysis (von Storch et al. 1995) was performed on the model interface depths. POP analysis searches a dataset for linear oscillatory modes and produces a spatial pattern, oscillation time scale, and decay period for each mode. The spatial pattern is complex, with the real and imaginary parts of the pattern representing two phases of the oscillation in quadrature. The patterns can be thought of as snapshots of the oscillation in time, proceeding as Im > Re > −Im > −Re > Im over the

TABLE 1. Significant POP mode characteristics from the 2° model analysis.

Period (yr)	Decay time (yr)	% variance
4.94	23.0	26.6
8.07	17.4	19.9
12.5	24.2	17.0
4.14	9.96	16.1

period of the POP mode, where Im is the imaginary component of the pattern and Re the real component.

First, the layer interface depth fields were taken and the monthly means were removed to generate an anomaly time series. Next, a least squares linear trend in time was removed from the field. Then the time series of each layer was normalized by the interface's reduced gravity. This was done in order to ensure that the dynamics of each model level would contribute equally to the analysis; otherwise, the surface field (variance $\sim$5–70 $\times$ 10^{-4} m^2) would contribute to the POP analysis much less than the deeper layers (variance $\sim$50–350 m^2), even though the sea surface height has a major influence on the system's dynamics.

EOF decomposition was then performed on these normalized anomalies, and EOF modes containing 80% of the total variability were retained for the POP analysis. Adding more or fewer EOF modes to the POP analysis had little impact on the analysis results. Once the POP modes were constructed, each model layer was denormalized to restore their proper relative magnitudes.

The POP analysis of the 2° model produces 12 modes, 4 of which are significant (Table 1); in contrast, the 1° model produces 23 modes, none of which are significant, as they only project onto small portions of the gyre. This emphasizes that the 2° oscillation is a coherent, gyre-spanning phenomena, while the 1° model's variability is much more localized. The longest-period mode of the 2° model has its largest projection in the Central Mode Water area and appears to be related to changes in the Kuroshio Extension position and long-term variations in the subduction rate. The shorter-period modes are fairly evenly spread around the gyre, and clearly represent components of the oscillation's variability. The wide range of time scales in the shorter-period modes (4–8 yr) probably indicates the oscillation dynamics are nonlinear. Short-period modes have smaller spatial anomalies than long-period modes.

Examination of the physical structure of the highest-variance POP mode suggests two possible driving mechanisms for the oscillation (Fig. 2). The vertical structure of the oscillation near the Central Mode Water outcrop is confined to the upper layers, suggesting it is driven in this region by changes in the subduction rate. Conversely, in the westward flow of the subtropical gyre the oscillation extends throughout the water column with a first-mode baroclinic structure. The vertical phase lines of this structure are backward-leaning, with the deep anomalies leading the surface anomalies by $\sim$250 km along path. The other POP modes also display this structure. This is a signature of baroclinic instability, suggesting that unstable flows may play a role in amplifying the anomalies as they propagate westward.

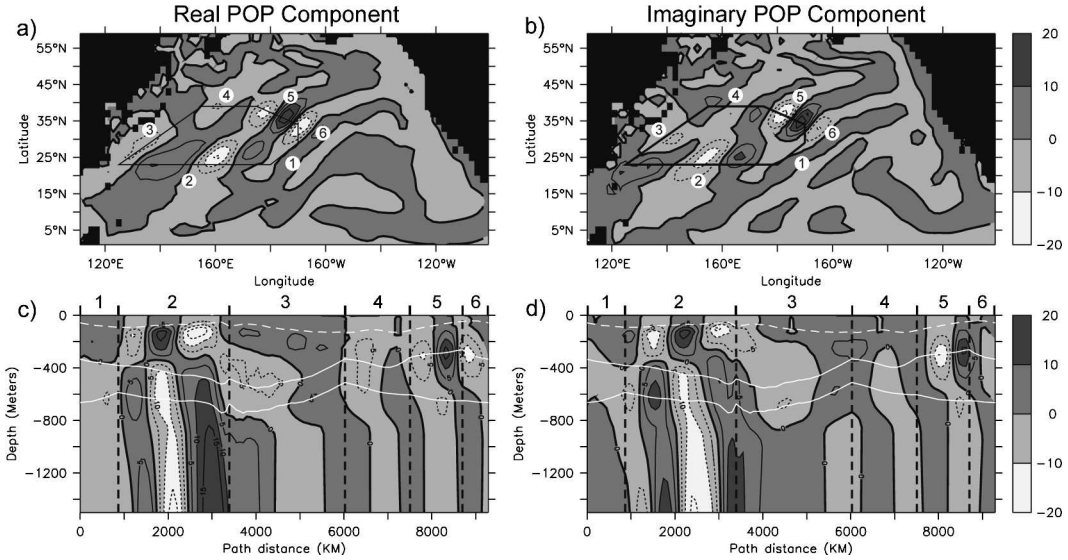

FIG. 2. Spatial projection of the leading POP mode of layer interface in the 2° model (m): (left) the real component of the POP mode and (right) the imaginary. (a) Magnitude of POP mode on the 26.5-σ_θ isopycnal (m). The path defined in Fig. 1 is drawn in black. Numerical labels correspond to labels in (b). (b) Magnitude of POP mode (m) along a vertical section defined by the path in (a), starting at 30°N, 170°W and proceeding clockwise. Vertical black dashed lines mark turns in the path, with numerical labels corresponding to labels in (a). Solid white lines denote top and bottom of 26.5-σ_θ isopycnal; dashed white line denotes depth of mixed layer.

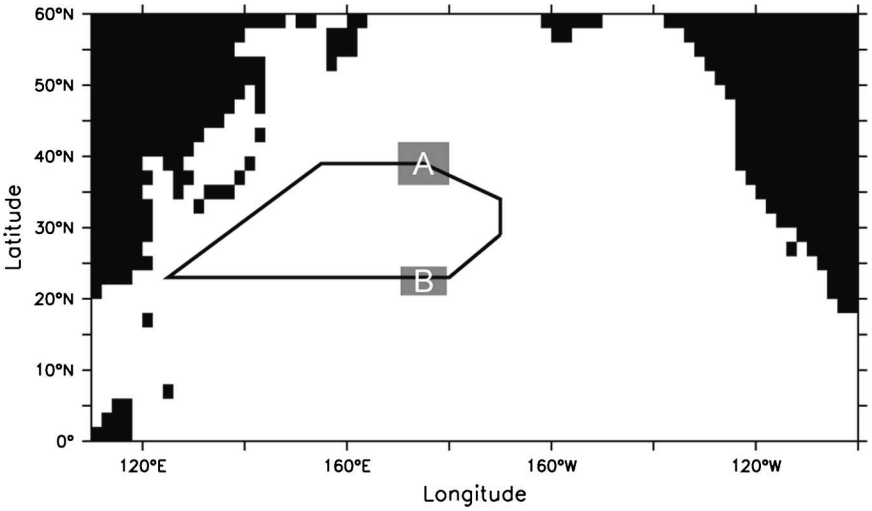

FIG. 3. Averaging locations for subduction rate (A) and instability calculations (B). Black line denotes path from Figs. 1 and 2.

c. Subduction covariances

To examine the role that subduction in the Central Mode Water region plays in the oscillation, a subduction index was calculated. This was taken as the average annual fluid flux into the 26.5-σ_θ layer over the area 36°–42°N, 170°E–180° (Fig. 3), normalized by the standard deviation of the time series. This area is the region of maximum variance in the model's subduction rate. Lag and lead covariances between this index and the 26.5-σ_θ layer thickness anomaly around the anomaly path were then taken (Fig. 4). If there is strong correlation when the subduction rate lags the layer-thickness anomaly time series, it indicates the layer-thickness anomalies are influencing the subduction rate, most likely by altering the stratification at the wintertime outcrop. On the other hand, if there is strong correlation when the subduction rate leads the layer thickness, it indicates that the rate of anomalous subduction controls the generation of layer-thickness anomalies in the central mode water area. We see significant correlations when the subduction rate lags the layer thickness,

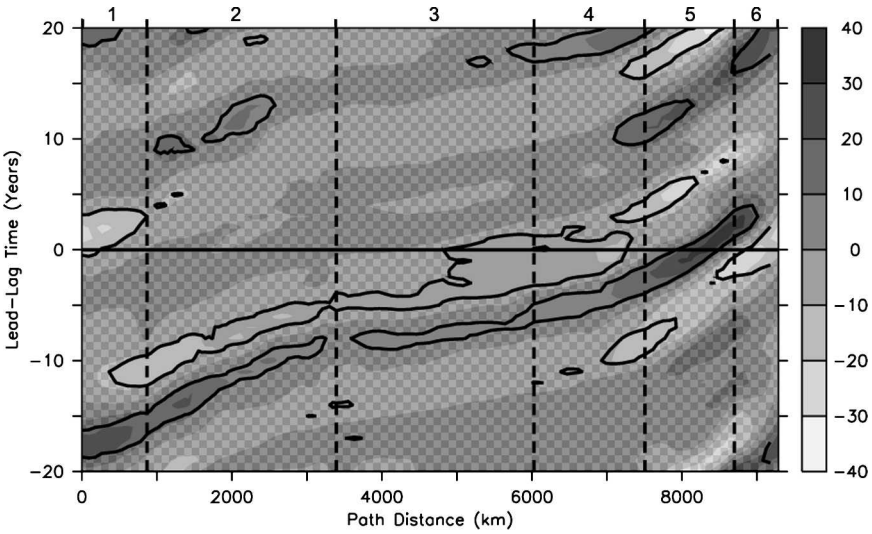

FIG. 4. Lead–lag covariance of isopycnal thickness anomaly along oscillation path (as defined in Fig. 3) with Central Mode Water subduction rate (m). Undotted area surrounded by black contour is significantly correlated at the 95% confidence level. Vertical dashed lines mark turns in the path. The area over which the subduction rate is calculated is situated between sections 4 and 5 of the path. The subduction rate is calculated as the amount of water entering layer 7 from the surface, normalized by the std dev of the subduction time series.

which suggests that the thickness anomalies are controlling the subduction rate, not vice versa.

4. Model instability characteristics

a. Quasigeostrophic instability analysis

The major problem with the idea that baroclinic instability drives the oscillation is the large spatial scale of the anomalies. Baroclinic instability usually occurs on the scale of the Rossby radius, almost two orders of magnitude smaller than the size of the model anomalies, since the beta effect suppresses the growth of large-scale instabilities. If instability is driving the flow, we must explain why the flow is unstable at such large length scales.

To examine the possibility of flow instability acting as a driving force in the oscillation, a quasigeostrophic oscillatory mode decomposition was performed on the model, following Pedlosky (1987). First, a vertically varying zonal background flow is assumed for the streamfunction, $\Psi_n = -U_n y$, where n indicates the model layer, numbered from surface to bottom. The background potential vorticity is taken to be

$$q_1 = f + \beta y + \nabla^2\Psi_1 - \frac{\Psi_1}{\lambda_{1,1}^2} + \frac{(\Psi_2 - \Psi_1)}{\lambda_{2,1}^2}, \tag{1a}$$

$$q_n = f + \beta y + \nabla^2\Psi_n + \frac{(\Psi_{n+1} - \Psi_n)}{\lambda_{n+1,n}^2} + \frac{(\Psi_{n-1} - \Psi_n)}{\lambda_{n,n}^2}, \tag{1b}$$

and

$$q_{10} = f + \alpha y + \beta y + \nabla^2\Psi_{10} + \frac{(\Psi_9 - \Psi_{10})}{\lambda_{10,10}^2}, \tag{1c}$$

where

$$\lambda_{n,m}^2 = g_n' h_m / f^2. \tag{2}$$

Here f is the Coriolis parameter at a reference latitude, β is the meridional gradient of the Coriolis parameter, ∇^2 is the horizontal Laplacian operator, α is the meridional topography slope, g_n' is the reduced gravity of the nth interface, and h_m is the thickness of the mth layer. These equations are then substituted into the potential vorticity tendency equation,

$$\frac{\partial q_n}{\partial t} + U_n \frac{\partial q_n}{\partial x} + \frac{\partial \Psi_n}{\partial x}\frac{\partial q_n}{\partial y} = 0; \tag{3}$$

Ψ_n is then perturbed by adding a small sinusoidal disturbance of the form

$$\phi_n = \mathrm{Re}[A_n e^{-i(\omega t - kx)}], \tag{4}$$

where ω is the frequency of the disturbance (s^{-1}), k is the disturbance's wavenumber (m^{-1}), and A_n is the complex amplitude of the disturbance ($m^2\ s^{-1}$). With some manipulation, the perturbed Eq. (3) can be rewritten in matrix form as

$$i\omega \mathbf{A}\boldsymbol{\phi} = \mathbf{B}\boldsymbol{\phi}, \tag{5}$$

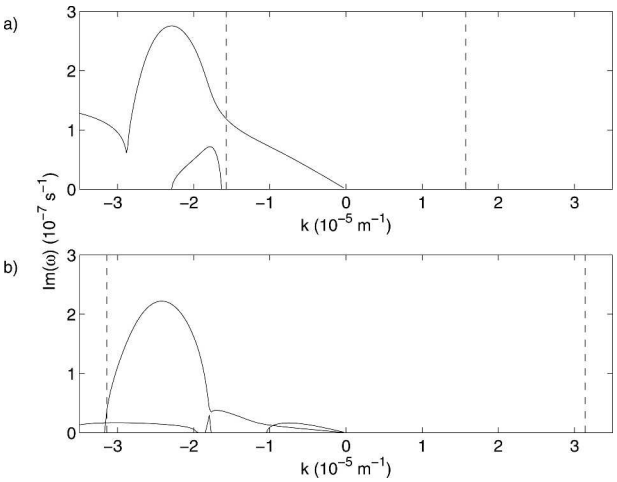

FIG. 5. Imaginary component of ω as a function of k, calculated for (a) 1° and (b) 2° resolution. Vertical dashed line indicates the Nyquist wavenumber for each resolution. Positive wavenumbers point eastward.

where iω is the negative of the time derivative, **A** transforms the streamfunction into PV, and **B** represents the linearized advection terms of the PV equation. Both **A** and **B** are functions of k. Multiplying both sides by $-i$ $\mathbf{A}^{-1}$ produces an eigenvalue equation for ω,

$$-i\mathbf{A}^{-1}\mathbf{B}\boldsymbol{\phi} = \omega\boldsymbol{\phi}, \tag{6}$$

which is then solved for a range of k to produce a dispersion relationship for the disturbance. Since there are 10 vertical layers in the model, 10 eigenvalues are produced for each k; in the absence of a background velocity field, these would simply be the barotropic and nine baroclinic Rossby wave modes. Complex eigenvalues represent unstable modes. Note that the analysis presented here assumes continuous fields, in contrast to the discretized equations employed by HIM. The analysis was also performed with a discretized framework, with similar results to the continuous case. Thus, in the interests of general applicability and familiarity, only the continuous analysis is presented here.

The average layer velocities, thickness, and reduced gravities were calculated for the region 20°–25°N, 170°E–180° (Fig. 3) in the 2° and 1° models, and the ω values calculated for various k in each case. The results show an instability present at all small negative wavenumbers (Fig. 5) in both models, which represents westward-traveling, long-wavelength instability. This instability appears to be of the same type discussed by Qiu (1999), having a two-layer structure in the thermocline and very little projection on the deep layers below. The meridional slope of the base of the thermocline acts in a manner similar to a topographic slope, creating a potential vorticity gradient in the upper layers that cancels the effect of β and allows longwave instabilities to appear. In other words, we have a kind of two-layer baro-

clinic instability that treats the thermocline as the effective depth of the ocean.

While both the 2° and 1° models are unstable at all long wavelengths, the 1° model's higher resolution permits the existence of a smaller-scale, faster-growing instability with $k \sim -(2\text{–}3) \times 10^{-5}$ m^{-1} (Fig. 5b). The resolving of this smaller-scale mode is a possible explanation for the disappearance of the oscillation at higher resolution, as the smaller eddies could disrupt the physical structure of the larger-scale oscillation (Drijfhout 1992). However, the instabilities that appear in the 2° model are clearly not the same length scale as that of the fastest-growing mode that appears in the instability analysis. The model instabilities have a $k \sim -2 \times 10^{-6}$ m^{-1}, and the fastest growing mode from the instability analysis is at the horizontal resolution cutoff of the model, $k = -1.7 \times 10^{-5}$ m^{-1}. The preferred length scale of the instability must still be explained.

b. Effect of viscosity

The model viscosity is the final difference between the two runs. Higher-resolution models tend to have lower viscosities because of numerical instability considerations and the need to resolve the western boundary currents. However, viscosity preferentially works on small spatial scales, working to smooth roughness in the velocity field and to create coherent, large-scale flows. This imposes a kind of effective shortwave resolution cutoff on model instabilities, which may be stricter than the limits imposed by the model's grid spacing. The shorter the wavelength of an instability, the faster it must grow to overcome the viscous dissipation, and thus only longer-wavelength instabilities can appear in high-viscosity models.

Equation (3) is easily modified to take into account the effects of viscosity. It becomes

$$\frac{\partial q_n}{\partial t} + U_n \frac{\partial q_n}{\partial x} + \frac{\partial \Psi_n}{\partial x}\frac{\partial q_n}{\partial y} = -A_H \nabla^6 \Psi_n, \qquad (7)$$

where ∇^6 is the Laplacian of the biharmonic operator and A_H is the diffusivity (m^4 s^{-1}), used since the model implements a biharmonic viscosity. The remaining steps of the instability analysis are basically unchanged by this addition.

Using the 2° model's biharmonic diffusivity of 1.5×10^{15} m^4 s^{-1} in this analysis results in a very different pattern of unstable wavenumbers (Fig. 6a). The viscosity damps all instabilities with wavenumbers larger than $\sim 10^{-5}$ m^{-1}, corresponding to a wavelength of ~600 km. The fastest-growing wavelength is now ~1500 km, which agrees much better with the oscillation scale observed in the model output. This analysis was also performed using a Laplacian viscosity of 6.5×10^4 m^2 s^{-1}, chosen to have a comparable dissipation time at the grid scale with the biharmonic viscosity above. This change did not significantly affect the results. The 1° model also shows a significantly altered instability diagram when the effects of viscosity are included (Fig. 6b). Shortwave instabilities are damped, but not as harshly as in the 2° model, allowing smaller-scale structures to form.

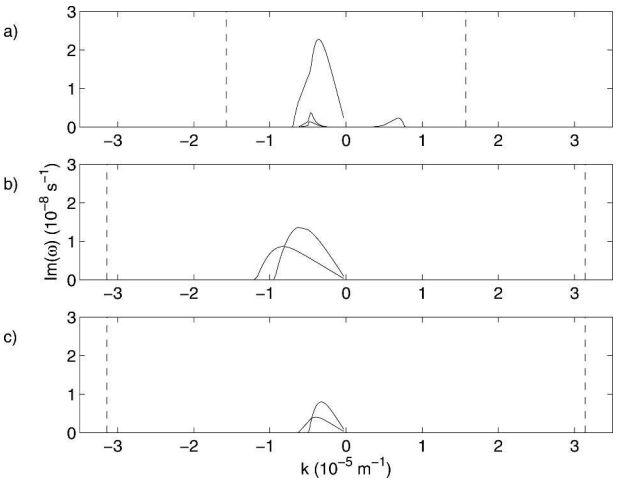

FIG. 6. Imaginary component of ω as a function of k, calculated with biharmonic viscosity included for the (a) 2° model, $A_H = 1.5 \times 10^{15}$ m^4 s^{-1}; and the 1° model at (b) low, $A_H = 4.1 \times 10^{13}$ m^4 s^{-1}, and (c) high, $A_H = 1.5 \times 10^{15}$ m^4 s^{-1}, viscosity. Note that the vertical scale is a factor of 10 smaller than that in Fig. 5. Vertical dashed lines indicate the Nyquist wavenumber in each case.

Last, we performed the instability analysis on the 1° model but used the 2° model's viscosity (Fig. 6c). This produced an instability diagram very similar to the 2° model's. Thus, we can check the validity of this analysis by running the 1° model with the 2° model's viscosity. If viscosity is the controlling factor for the resolution of instabilities, then this should make the 1° model exhibit gyre-scale variability in the same manner as the 2° model. Running the spunup 1° model with the 2° model's viscosity indeed produces oscillations as in the 2° model, lending credence to this idea.

We do not mean to suggest here that quasigeostrophic instability in the STCC is the sole driver of this oscillation—merely that it is the instigator. The viscosity decay time for a quasigeostrophic wave in the 2° model is ~1 month—free waves clearly cannot make a 25-yr transit around the gyre, and must be re-enforced by local instability growth or feedback mechanisms such as modulation of the CMW subduction rate. Because of the difficulties inherent in performing a modal decomposition on a meridional current, we are unable to show analytically that anomalies generated in the STCC could propagate around the gyre without being dissipated, and must rely on the evidence of Figs. 1–4 to support the assertion that the anomalies maintain their identity as they progress around the path.

5. Viscosity and effective resolution

Here we derive a relationship determining if an instability of a given length scale is permitted by a mod-

el's viscosity. As a starting point we take the Reynolds instability criterion for a biharmonic viscosity as defined by Griffies and Hallberg (2000),

$$A_H > \frac{U\Delta^3}{16}, \tag{8}$$

where U is a representative velocity scale for the model (m s^{-1}) and Δ is the maximum grid spacing in meters; A_H larger than this criterion are necessary to suppress numerical noise due to failure to resolve grid-scale turbulence. For eddy-resolving scales this is a stricter bound on the minimum viscosity than the criterion for resolution of the western boundary currents ($A_H > \beta\Delta^5$; Griffies and Hallberg 2000).

The e-folding decay rate due to viscosity for a sinusoidal geostrophic disturbance is given by

$$\omega(k^2 + \lambda^{-2}) = A_H k^6, \tag{9}$$

where ω is the decay rate (s^{-1}), k is the horizontal wavenumber of the disturbance (m^{-1}), and λ is the Rossby radius for a given vertical mode (m). Using (8) as the value of A_H in (9) gives

$$\omega = \frac{U\Delta^3 k^6}{16(k^2 + \lambda^{-2})}. \tag{10}$$

Here, ω represents the viscous decay rate a geostrophic structure with wavenumber k will experience at a resolution of Δ. To resolve a given instability, we want the growth rate of the instability to be significantly greater than this viscosity decay rate. Note that a similar relationship for Laplacian viscosity is easily derivable, as is one using the western boundary current condition for minimum viscosity.

As an example of the utility of this equation, we calculate the resolution needed to resolve baroclinic instability in the western boundary currents. These instabilities are characterized by e-folding growth times on the order of a few months and length scales of order 150 km. We take a decay time of 1 yr to be the borderline decay regime that would allow normal instability dynamics. Taking $U = 1$ m s^{-1}, $\lambda = 33$ km, $k = 2\pi(150$ km$)^{-1}$ and $\omega = 2\pi(1$ yr$)^{-1}$ gives $\Delta = 11.6$ km, or $\sim$1/10° resolution, which is the model grid resolution at which realistic western boundary current separation begins to appear (Griffies et al. 2000).

Quasigeostrophic instability growth time scales in the World Ocean are on the order of 3 months (Gill et al. 1974). We assume a 5-yr decay time is small enough to permit full resolution of the geostrophic wave dynamics. However, a 1-yr decay time is probably sufficient to allow for more vigorous ocean dynamics, such as in the western boundary currents. A 1-month decay time serves as a hard cutoff, past which point viscosity completely dominates the ocean dynamics. Substituting these values for ω in (10) and rearranging allows us to write a set of relationships between k and Δ, representing the grid spacing needed to resolve a given wavenumber:

$$\Delta^3 = \frac{16\omega}{U}\frac{(k^2 + \lambda^{-2})}{k^6}. \tag{11}$$

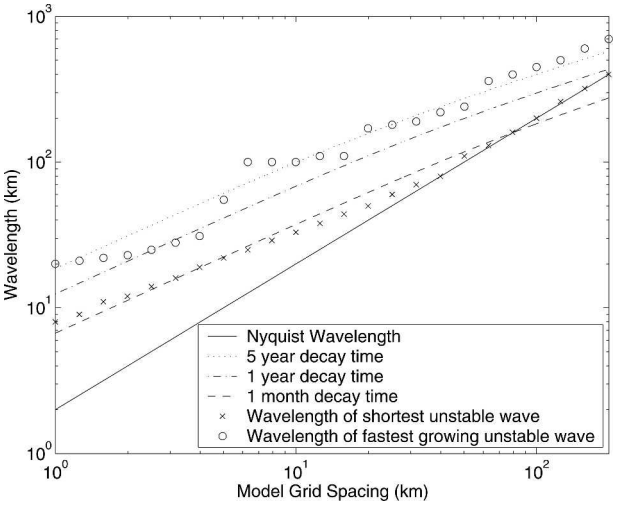

FIG. 7. Decay rates of zonal geostrophic waves at various model resolutions. Wavelengths below the solid black line are not resolved by the model grid spacing. Broken lines represent (11) calculated with various viscous decay rates; o and x points are taken from a quasigeostrophic instability analysis using data from the *WOA94* climatology (Levitus et al. 1994) and biharmonic viscosities compatible with a given model resolution.

To examine the actual applicability of (11), a quasigeostrophic instability analysis of real ocean data was performed. Physical quantities for the instability analysis were taken from the Levitus climatology, and the analysis performed was identical to the one in section 4b, save that 20 vertical layers were used. Geostrophic velocity was calculated assuming a layer of no motion at 2-km depth. The analysis was performed for a range of viscosities, calculated from (8) to be representative of various model grid spacings; U was taken to be 0.05 m s^{-1}, slightly larger than the maximum velocity in the averaged area. To measure the length scale resolved by the viscosities, two values were used: the wavelength of maximum instability growth, and the smallest wavelength wave that was unstable. These results show good agreement with (11) (Fig. 7). Note this result does not apply at the equator, where f-plane quasigeostrophy does not hold, and that λ and U can vary widely depending upon the region of the ocean examined. We have taken a local U value here, but models incorporating the western boundary currents could easily have U values of 1 m s^{-1}, making the resolving power of the model much worse.

The primary result of (11) is that the physical length scale resolved by a model is not linearly related to the grid spacing. For wavelengths smaller than the Rossby radius, (11) indicates a $\Delta^{3/4}$ relationship between grid

spacing and the length scale of the instability that is resolved. For wavelength larger than the Rossby radius, the situation is even worse; there, the resolved length scale increases as $\Delta^{1/2}$. A least squares best fit to the smallest unstable wavelength data from the analysis of the *WOA94* climatology (x in Fig. 7) indicates a $\Delta^{3/5}$ relationship. This means that doubling grid spacing only improves resolution by a factor somewhere between 1.4 and 1.7. Therefore, it soon may be more computationally efficient to improve model resolution by improving the formulation of the viscosity operator, rather than simply increasing the number of model grid points. Use of a Smagorinsky-type viscosity (Griffies and Hallberg 2000), which effectively recalculates (8) using a local U at each time step, would obviously be helpful in this regard.

6. Conclusions

An isopycnal ocean model that displays a gyre-scale oscillation at 2° resolution that vanishes when the model is run at 1° resolution was presented. POP analysis of the 2° oscillation statistically confirms it can be considered as a coherent gyre-scale structure and suggests two driving mechanisms: subduction variance in the Central Mode Water region, and geostrophic instability in the Subtropical Countercurrent. Lead–lag correlations between the CMW subduction rate and the 26.5-σ_θ layer thickness anomaly along the oscillation path indicate that thickness anomalies entering the CMW area are driving variation in the CMW subduction rate. Thus, instability in the STCC is the prime candidate for the source of the oscillatory behavior.

A quasigeostrophic potential vorticity instability analysis of the mean model state in the STCC near the date line shows a long-wavelength instability present that is similar to the instability described by Qiu (1999). However, to explain the preferred length scale of the model instability, the effects of horizontal viscosity must be taken into account. A biharmonic viscosity term added to the QGPV analysis creates an effective shortwave resolution cutoff, permitting large-scale instabilities, which normally would be disrupted by smaller-scale eddy activity, to grow. This is supported by the reappearance of the oscillation when the 1° model is run with its viscosity increased to match the 2° model. Last, a condition for the grid spacing necessary to resolve instabilities of a given length and time scale is derived. This condition indicates that model resolution increases as a fractional power of the grid spacing, rather than linearly.

Numerical modeling is essentially the study of the nonlinearities of the ocean; we model the instabilities and other advective phenomena that do not appear in linear models of the circulation. The current viscosity schemes used by models hamper this study by effectively decreasing the Reynolds number of the mesoscale. As remarked by Griffies et al. (2000), there is currently no plausible theory to motivate the current frictional operators used in ocean climate models. Using better parameterizations of horizontal viscosity holds the possibility of dramatic improvements in the resolution of models with fine grid spacing.

Instability diagrams for small regions of the ocean that appear unstable can be a useful tool in evaluating the robustness of model oscillations but are difficult to use in larger-scale systems because of the assumptions of uniform shear and layer structure that are used to make the analysis tractable. A better method may be to run the model at higher resolution to verify the convergence of the solution. For example, we performed a run at 1/3° that was initialized from the spunup 2° model fields. It required only a year of model time to verify that the anomalies were rapidly sheared apart by smaller-scale baroclinic instability. It is likely that a short run at double resolution would be sufficient to evaluate an oscillation's robustness.

The fact that eddy-resolving resolution is needed to accurately model western boundary currents, and thus ocean heat budgets, is well known (Hurlburt and Hogan 2000; Oschlies 2002), but this study indicates the possibility that modeling at low resolution, and thus higher viscosity, can introduce spurious oscillations to the system. This indicates that higher resolution may not just be desirable for decadal climate models; it may be vital. At the very least, care should be taken in examining the oscillations that appear in climate models, and protocols for verifying these oscillations should be developed.

Acknowledgments. We acknowledge programming help from David Darr, assistance with the model code from Robert Hallberg, and useful discussions with Susan Hautala. We also thank Arthur Miller and an anonymous reviewer whose comments improved the manuscript. This material is based upon work supported by the National Science Foundation under Grants 9818920 and 0095106.

REFERENCES

Best, S. E., V. O. Ivchenko, K. J. Richards, R. D. Smith, and R. C. Malone, 1999: Eddies in numerical models of the Antarctic Circumpolar Current and their influence on the mean flow. *J. Phys. Oceanogr.,* **29,** 328–350.

Böning, C. W., and R. G. Budich, 1992: Eddy dynamics in a primitive equation model: Sensitivity to horizontal resolution and friction. *J. Phys. Oceanogr.,* **22,** 361–381.

Colin de Verdiere, A., and T. Huck, 1999: Baroclinic instability: An oceanic wavemaker for interdecadal variability. *J. Phys. Oceanogr.,* **29,** 893–910.

Cox, M. D., 1987: An eddy-resolving numerical model of the ventilated thermocline: Time dependence. *J. Phys. Oceanogr.,* **17,** 1044–1056.

Da Silva, A. M., C. C. Young, and S. Levitus, 1994: *Algorithms and Procedures.* Vol. 1, *Atlas of Surface Marine Data 1994,* NOAA Atlas NESDIS 6, 51 pp.

Dommenget, D., and M. Latif, 2002: Analysis of observed and

simulated SST spectra in the midlatitudes. *Climate Dyn.,* **19,** 277–288.

Drijfhout, S. S., 1992: Ring genesis and the related heat transport. Part II: A model comparison. *J. Phys. Oceanogr.,* **22,** 268–285.

Frankignoul, C., 1985: Sea surface temperature anomalies, planetary waves, and air-sea feedback in the middle latitudes. *Rev. Geophys.,* **23,** 357–390.

Gill, A. E., J. S. A. Green, and A. J. Simmons, 1974: Energy partition in the large-scale ocean circulation and the production of mid-ocean eddies. *Deep-Sea Res.,* **21,** 499–528.

Griffies, S. M., and R. W. Hallberg, 2000: Biharmonic friction with a Smagorinsky-like viscosity for use in large-scale eddy-permitting ocean models. *Mon. Wea. Rev.,* **128,** 2935–2946.

——, and Coauthors, 2000: Developments in ocean climate modelling. *Ocean Modell.,* **2,** 123–192.

Griffiths, C., M. Ikeda, and P. C. Smith, 2000: A numerical model comparison of baroclinic instability in the presence of topography. *Tellus,* **52A,** 42–65.

Gu, D. F., and S. G. H. Philander, 1997: Interdecadal climate fluctuations that depend on exchanges between the Tropics and extratropics. *Science,* **275,** 805–807.

Hallberg, R., 1995: Some aspects of the circulation in ocean basins with isopycnals intersecting the sloping boundaries. Ph.D. thesis, University of Washington, 244 pp.

Hazeleger, W., and S. S. Drijfhout, 2000: A model study on internally generated variability in subtropical mode water formation. *J. Geophys. Res.,* **105,** 13 965–13 979.

Hurlburt, H. E., and P. J. Hogan, 2000: Impact of 1/8° to 1/64° resolution on Gulf Stream model-data comparisons in basin-scale subtropical Atlantic Ocean models. *Dyn. Atmos. Oceans,* **32,** 283–329.

Kobashi, F., and H. Kawamura, 2001: Variation of sea surface height at periods of 65–220 days in the subtropical gyre of the North Pacific. *J. Geophys. Res.,* **106,** 26 817–26 831.

Ladd, C. A., and L. Thompson, 2002: Decadal variability of North Pacific Central Mode Water. *J. Phys. Oceanogr.,* **32,** 2870–2881.

Latif, M., and T. Barnett, 1994: Causes of decadal climate variability over the North Pacific and North America. *Science,* **266,** 634–637.

Levitus, S., and T. P. Boyer, 1994: *Temperature.* Vol. 4, *World Ocean Atlas 1994*, NOAA Atlas NESDIS 4, 117 pp.

——, R. Burgett, and T. P. Boyer, 1994: *Salinity.* Vol. 3, *World Ocean Atlas 1994*, NOAA Atlas NESDIS 3, 99 pp.

Oberhuber, J. M., 1993: Simulation of the Atlantic circulation with a coupled sea ice–mixed layer–isopycnal general circulation model. Part I: Model description. *J. Phys. Oceanogr.,* **23,** 808–829.

Oschlies, A., 2002: Improved representation of upper-ocean dynamics and mixed layer depths in a model of the North Atlantic on switching from eddy-permitting to eddy-resolving grid resolution. *J. Phys. Oceanogr.,* **32,** 2277–2298.

Pedlosky, J., 1987: *Geophysical Fluid Dynamics.* Springer-Verlag, 710 pp.

Qiu, B., 1999: Seasonal eddy field modulation of the North Pacific Subtropical Countercurrent: TOPEX/Poseidon observations and theory. *J. Phys. Oceanogr.,* **29,** 2471–2486.

——, 2000: Interannual variability of the Kuroshio Extension system and its impact on the wintertime SST field. *J. Phys. Oceanogr.,* **30,** 1486–1502.

——, 2002: The Kuroshio Extension system: Its large-scale variability and role in the midlatitude ocean–atmosphere interaction. *J. Oceanogr.,* **58,** 57–75.

——, and W. Miao, 2000: Kuroshio path variations south of Japan: Bimodality as a self-sustained internal oscillation. *J. Phys. Oceanogr.,* **30,** 2124–2137.

Tai, C.-K., and W. White, 1990: Eddy variability in the Kuroshio Extension as revealed by *Geosat* altimetry: Energy propagation away from the jet, Reynolds stress, and seasonal cycle. *J. Phys. Oceanogr.,* **20,** 1761–1777.

von Storch, H., G. Bürger, R. Schnur, and J.-S. von Storch, 1995: Principal oscillation patterns: A review. *J. Climate,* **8,** 377–400.

Wood, R. A., and M. Ikeda, 1994: Comparison of mesoscale meanders and eddies simulated by quasi-geostrophic and primitive equation models: A case study. *J. Geophys. Res.,* **99,** 22 645–22 663.

Zeng, X., M. Zhao, and R. E. Dickinson, 1998: Intercomparison of bulk aerodynamic algorithms for the computation of sea surface fluxes using TOGA COARE and TAO data. *J. Climate,* **11,** 2628–2644.